Supporting Information: Ultrafast Spin Crossover in a Room-Temperature Ferrimagnet: Element-Specific Spin Dynamics in Photoexcited Cobalt Ferrite

Stephen Londo,[†] Somnath Biswas,[†] Jakub Husek,[†] Igor V. Pinchuk,[‡] Michael J. Newburger,[‡] Alexandra Boyadzhiev,[‡] Amanda H. Trout,[¶,§] David W. McComb,[¶,§] Roland Kawakami,[‡] and L. Robert Baker*[,†]

†*Department of Chemistry and Biochemistry, The Ohio State University, Columbus, Ohio 43210, USA*

‡*Department of Physics, The Ohio State University, Columbus, Ohio 43210, USA*

¶*Department of Materials Science and Engineering, The Ohio State University, Columbus, Ohio 43210, USA*

§*Center for Electron Microscopy and Analysis, The Ohio State University, Columbus, Ohio 43212, USA*

E-mail: baker.2364@osu.edu

Contents

1. Methods
2. Sample Characterization
3. Spectral Simulation

1. Methods

Sample Preparation

Cobalt ferrite (CFO) samples were grown in a molecular beam epitaxy (MBE) chamber with a base pressure of $\sim$ 1 x 10^{-10} torr. MgO(001) substrates were rinsed in de-ionized water and loaded into the MBE chamber. After a 30 minute anneal at 600 °C in vacuum, the substrate was cooled to 350 °C and a $\sim$ 5 nm MgO buffer layer was deposited from an e-beam evaporator at a rate of $\sim$ 0.1 nm/min. After cooling to 200 °C, an oxygen partial pressure of 5 x 10^{-7} was introduced and CFO films were grown by co-deposition of elemental Fe (99.99%) and Co (99.99%) from thermal effusion cells with a Fe:Co flux ratio of 2:1 as determined by a quartz deposition monitor. The overall CFO growth rate was typically $\sim$ 0.4 nm/min. *In situ* reflection high energy electron diffraction (RHEED) was used to monitor the sample surface throughout the growth and annealing process. These samples were presumed to be air stable and were stored in a nitrogen-purged chamber when not in use.

CFO deposited in this way thermodynamically takes on the inverse spinel structure, $[Fe^{3+}](Co^{2+}Fe^{3+})O_2$. Ideally, Fe^{3+} occupies all the tetrahedral sites and half of the octahedral sites and Co^{2+} occupies the remaining half of the octahedral sites. In practice, the inversion is not complete so that some of the Co^{2+} occupies the tetrahedral sites. Nevertheless, all metal centers are in the high-spin state and the tetrahedral sites are aligned anti-parallel to the octahedral sites, which are aligned parallel to each other.[S1] Below we show that XPS analysis supports a 0.77 degree of inversion for this material consistent with other reports for CFO.[S2–S5]

Transient XUV-RA Spectroscopy

Transient spectra were obtained under ultrahigh vacuum (10^{-9} torr) using extreme ultraviolet (XUV) light produced by tabletop high-harmonic generation. XUV harmonic probe

pulses are generated by focusing 35 fs, 800 nm light into a semi-infinite gas cell (SIGC) filled with He gas. 0.42 mJ of 400 nm light focused co-linearly with the 800 nm beam is used to break the inversion symmetry of the electric field, enabling the generation of both even and odd harmonics. A 0.65 μm Al foil (Lebow) is placed after the generation chamber to remove the 800 and 400 nm driving fields from the XUV probe pulse. The XUV beam is incident on a gold coated toroidal mirror, which focuses the beam onto the sample at 8° relative to the sample surface. The reflected XUV beam is then spectrally separated using an aberration-corrected concave variable line spaced grating and captured on a CCD camera (Andor, DO920P-BN).

CFO thin films are photoexcited using a pump fluence of 8.0 mJ per pulse per cm^2 centered at 400 nm at an incident angle of 20° relative to the sample surface. This pump beam is produced using second harmonic generation from the 800 nm fundamental. Time-resolved measurements are performed by measuring the XUV flux reflected from the sample with the pump beam on and off as a function of delay between the pump and probe pulses where the transient reflection-absorption (RA) spectrum is given by the pump-induced change in optical density (Equation 1). The time between delays is controlled by a retroreflector and delay stage (Newport, ILS150CC) with 1 μm bidirectional repeatability. A 0.2 μm Al foil (Lebow) is situated before the detector to block any scattered light from the pump beam. To prevent beam damage, the samples are rastered during experiments ensuring that no part is exposed to the pump beam for greater than 30 s. Each of the 60 time delays measured represents a total integration time of approximately 2,000 s amounting to 30 hours of total data collection time averaged over multiple samples.

$$\Delta OD = -log_{10}\left(\frac{I_{pump\,on}}{I_{pump\,off}}\right) \tag{1}$$

2. Sample Characterization

Atomic Force Microscopy

A Bruker AXS Dimension Icon Atomic Force Microscope (AFM) with ScanAsyst, equipped with a TESPA-V2 cantilever, was used to measure the surface roughness of CFO thin films. The AFM was operated in tapping mode at a resolution of 512 samples/line with 1.0 Hz scan rate over a 5 x 5 μm^2 area. The root-mean-square roughness (R_q) was determined to be 0.14 nm and was calculated using the NanoScope Analysis software.

High angle annular dark field STEM

Cross-section TEM lamella were prepared using a FEI Helios 600 dual beam focused ion beam instrument. A Ga^+ beam with accelerating voltages of 30 kV and 5kV was used for initial milling and thinning respectively. Final thinning was performed using a Fischione 1040 Ar Nanomill. High angle annular dark field scanning transmission electron microscopy (HAADF STEM) images were collected using a FEI probe-corrected Titan3 80-300 S/TEM operating at 300 kV.

Reflection High-Energy Electron Diffraction

The crystallinity of the sample surface was determined using reflection high-energy electron diffraction (RHEED). The RHEED pattern of the surface with the beam along the [110] azimuth is shown in Figure S1a. The sharp streaking pattern indicates a flat, single-crystal surface, in agreement with the HAADF STEM and AFM measurements in Figure 1 from the manuscript.

X-ray Photoelectron Spectroscopy

High resolution X-ray photoemission spectroscopy (XPS) analysis was performed on CFO thin films under ultrahigh vacuum (1.5 x 10^{-9} torr) using a Kratos Axis Ultra X-ray photoelectron spectrometer (monochromatic Al Kα X-ray source, E_{photon}=1486.6 eV). Figure S1 shows the XPS spectra and the associated fits for the O 1s (b), Fe 2p (c) and Co 2p (d) transitions using the CASA XPS software. All spectra are referenced to adventitious carbon at 284.5 eV. We assign the oxidation states for iron and cobalt to be 3+ and 2+, respectively, which is in good agreement with literature sources.[S5,S6] Table S1 has the fitting parameters used along with the percent contribution of each peak to the overall spectrum.

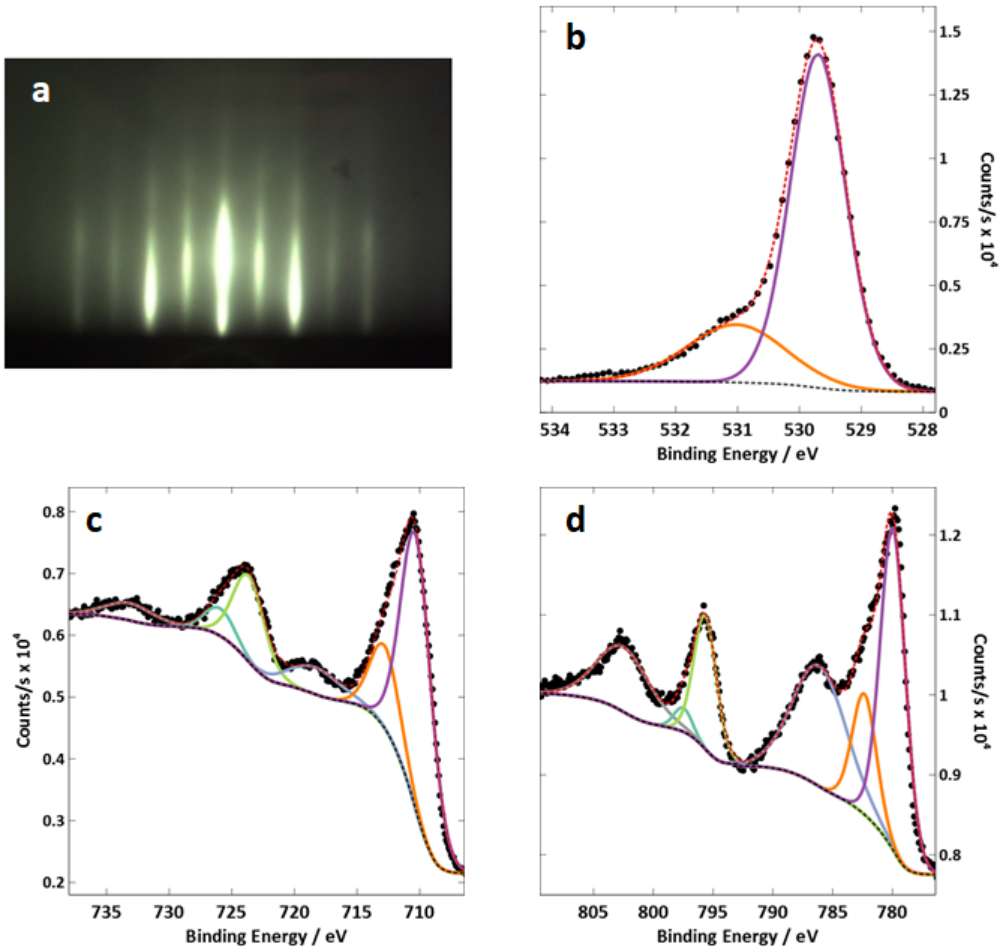

Figure S1: (a) RHEED measurements of 40 nm CFO films along the [110] azimuth. XPS measurements and the associated fits for the (b) O 1s, (c) Fe 2p, and (d) Co 2p transitions, respectively.

Table S1: The peak position (eV), width, and percent contribution to the overall spectrum in numerical ordering from lowest to highest energy of the XPS fitted peaks for the O 1s, Fe 2p, and Co 2p transitions.

	Peak 1			Peak 2			Peak 3			Peak 4			Peak 5			Peak 6		
	Position	Width	%	Position	Width	%	Position	Width	%	Position	Width	%	Position	Width	%	Position	Width	%
Iron	710.3	2.9	50.5%	712.8	2.8	14.7%	718.4	4.8	8.4%	723.6	3.0	16.5%	726.0	2.8	5.0%	733.2	4.5	5.0%
Cobalt	780.0	2.5	33.5%	782.3	2.4	12.0%	786.1	5.2	26.3%	795.7	2.3	12.5%	797.5	1.8	1.8%	802.5	5.2	14.0%
Oxygen	529.7	1.1	76.5%	531.0	1.9	23.5%	-	-	-	-	-	-	-	-	-	-	-	-

From the XPS data, we can estimate the inversion parameter by comparing the integrated area of the octahedral (O_h) and tetrahedral (T_d) contributions to the Co 2p spectrum. The peaks at 780 and 795.7 eV correspond to Co^{2+} in O_h sites, while the peaks at 782.3 and 797.5 eV correspond to Co^{2+} in T_d sites. By dividing the area for the O_h sites from the total area for both geometries, we find an inversion parameter of 0.77. This agrees well with what is found in literature, which can vary between ~ 0.70 and ~ 0.90 depending on preparation method.[S2–S5] Additionally, we can calculate the composition of the CFO thin films by summing the area underneath the $2p_{3/2}$ and $2p_{1/2}$ peaks for Fe and Co and taking the ratio adjusted for the atomic sensitivity factors. We find the Fe:Co ratio to be 1.5, indicating the CFO samples are slightly Co rich at the surface.

UV-Vis Absorption Spectroscopy

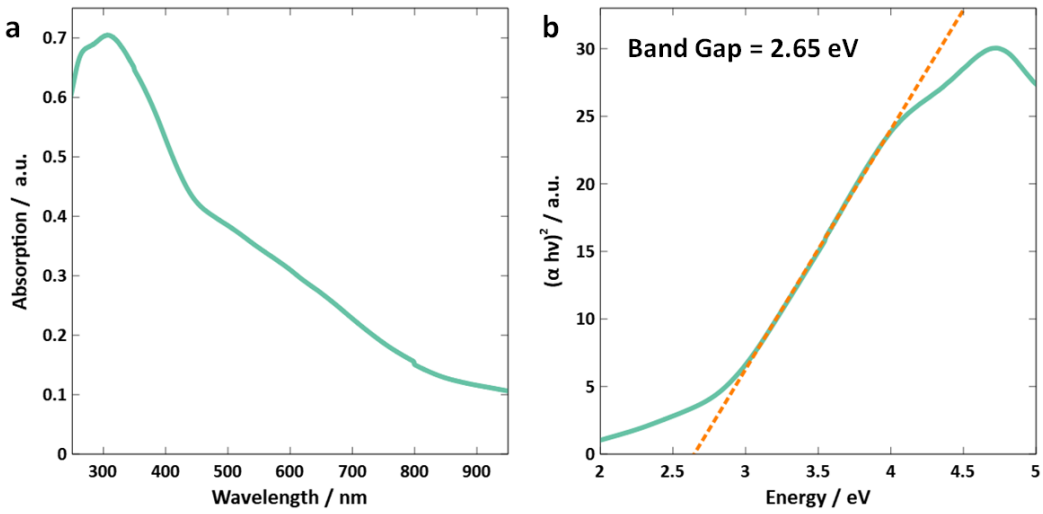

Figure S2: (a) Absorption spectrum of CFO thin films showing a large absorption band having an onset around 400 nm. (b) The absorption data converted into a Tauc plot with a calculated band gap excitation energy of 2.65 eV.

Absorption measurements of thin film CFO were obtained using a high performance Cary 5000 UV-Vis-NIR spectrophotometer from Agilent. Figure S2a shows the absorption spectrum between 200 - 1000 nm, which displays a large absorption feature having an onset around 400 nm. A clean MgO(001) 10 mm x 10 mm x 0.5 mm substrate was used to subtract the absorptive contribution of MgO. The absorption data was converted into a Tauc plot to determine the direct band gap excitation energy of this material (Figure S2b). A linear fit of $(\alpha h\nu)^2$ between 3 - 4 eV shows the direct band gap is 2.65 eV (the x-intercept of the linear fit). This is consistent with other CFO thin film samples, where the band gap varies based on fabrication method.[S7–S9]

Magnetic Hysteresis Analysis

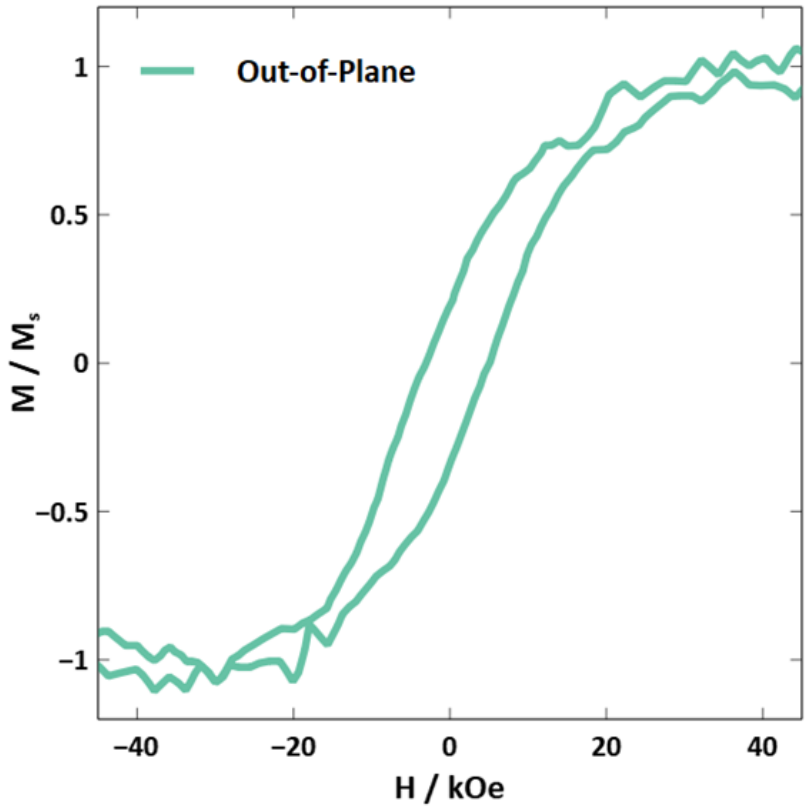

Figure S3: Out-of-plane magnetic hysteresis curves for CFO thin films using vibrating sample magnetometry at room temperature.

Magnetic properties of CFO thin films grown on MgO(001) were measured by vibrating sample magnetometry in a Quantum Design Physical Property Measurement System. The slightly larger lattice constant of the MgO substrate ($2a_{MgO}$ = 8.414 Å, a_{CFO} = 8.388 Å, 0.4% mismatch) produces tensile strain in the CFO film, leading to strain-induced perpendicular magnetic anisotropy. As shown in Figure S3, the out-of-plane magnetization loop measured at room temperature exhibits hysteresis with remanence of 26% and coercivity of 4.0 kOe. These magnetic properties are consistent with previously reported measurements of CFO.[S1,S10]

3. Spectral Simulation

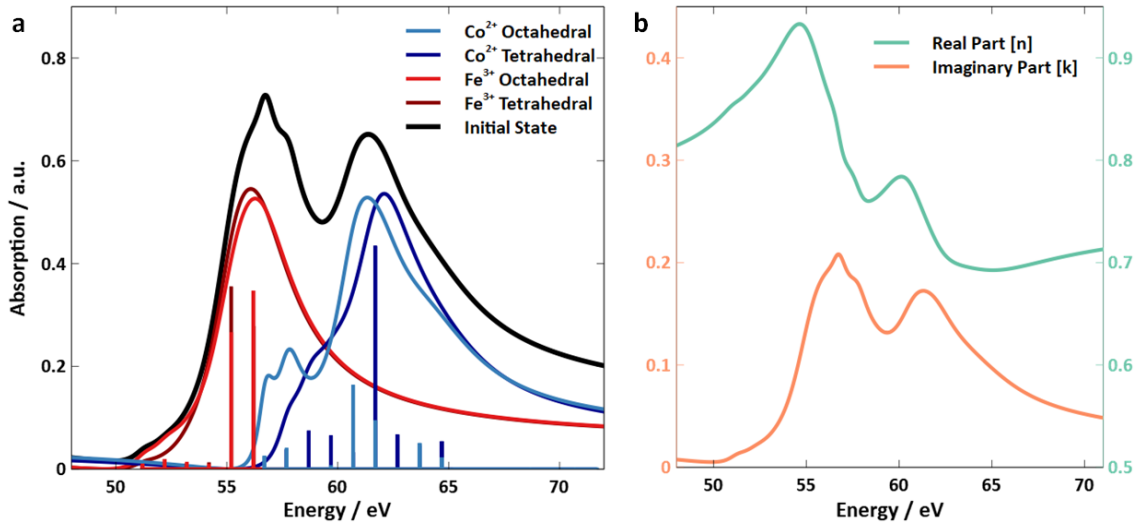

Figure S4: (a) Multiplet structures (stick spectra), absorption spectra and the weighted, combined absorption spectrum for the simulated CFO ground-state. (b) The resulting real and imaginary components of the refractive index from the weighted, combined spectrum.

In order to simulate XUV-RA spectra, we started by using the charge-transfer multiplet program CTM4XAS,[S11] which can calculate the atomic multiplet structures for transition metal ions in various oxidation states and ligand coordination environments. To generate a ground state spectrum, HS Fe^{3+} and Co^{2+} multiplet structures for both O_h and T_d configurations were simulated, represented by the stick spectra in Figure S4a. Lifetime broadening and Fano coupling parameters are introduced to the multiplet structures to generate absorption spectra (Figure S4a, solid lines). These are then scaled to absolute XUV absorption spectra for Fe_2O_3 [S12] and Co_3O_4 [S13] to convert the arbitrary CTM4XAS intensity units into absorption units for Fe^{3+} and Co^{2+}, respectively. Differences in the volumetric densities of absorption centers between the monometallic oxides and CFO as well as the degree of inversion (0.77) were quantitatively taken into account when summing the four individual absorption spectra, creating a representative ground state spectrum for bimetallic CFO (Figure S4a, black line).

Using Equation 2, the attenuation coefficient (α) is converted into the imaginary part

of the refractive index (k). From this, the real part of the refractive index is obtained by solving the Kramer-Kronig relationship (Equation 3), which relates the real part of a complex variable to its imaginary counterpart. In Equation 3, P denotes the Cauchy Principle value, which assigns a value to improper integrals that would otherwise be undefined. Materials are well known to experience a negative permittivity at these XUV frequencies.[S14,S15] This is accounted for by introducing a negative vertical offset to n as has been described previously.[S16] The resulting calculated values for k and n are shown in Figure S4b. These real and imaginary components are then combined to generate a complex refractive index ($\tilde{N}$), which is incorporated into the classical p-polarized Fresnel equation (Equation 4). This Fresnel equation is used to derive the reflectance spectrum where non-resonant XUV surface scattering is corrected for by introducing the Debye-Waller factor.[S17] The absolute square of reflectance gives reflectivity, whose negative logarithm is a reflection-absorption spectrum as shown in Equation 5. This resulting spectrum represents the ground state of CFO and is compared to the experimental ground state in Figure S5. The simulated spectra demonstrates good agreement with the experimental, have both the prominent Fe^{3+} absorption at 55 eV and the shoulder-like feature at 60 eV which corresponds to the Co^{2+} absorption edge.

$$\alpha = \frac{4\pi k}{\lambda} \tag{2}$$

$$n(\omega) = 1 + \frac{2P}{\pi}\int_0^\infty \frac{\omega' k(\omega')}{\omega'^2 - \omega^2} d\omega' \tag{3}$$

$$r = \frac{-\tilde{N}^2 cos(\theta) + \sqrt{\tilde{N}^2 - sin(\theta)^2}}{\tilde{N}^2 cos(\theta) + \sqrt{\tilde{N}^2 - sin(\theta)^2}} e^{\frac{-16\pi^2 R_q^2 cos(\theta)^2}{3\lambda^2}} \tag{4}$$

$$RA = -log_{10}(|r|^2) \tag{5}$$

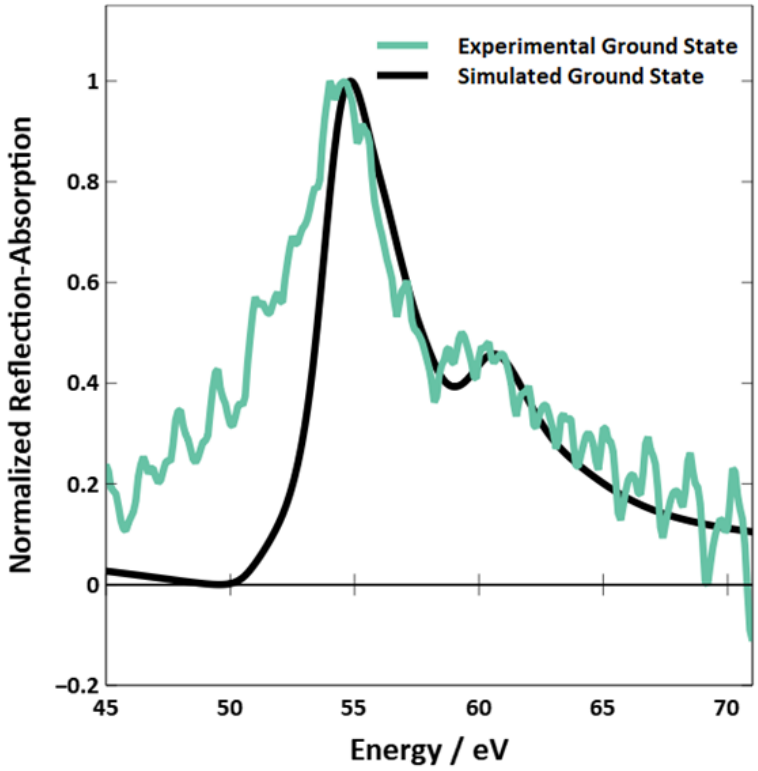

Figure S5: Simulated (black) and experimental (teal) ground state reflection-absorption spectra of CFO. A baseline offset has been applied to the experimental spectrum to correct for the photoemission background.

Given the 0.77 degree of inversion in these samples, there are four distinct $Co^{2+}/Fe^{3+} \rightarrow Co^{3+}/Fe^{2+}$ metal-to-metal charge transfer pathways to consider: (1) $Co^{2+}_{O_h}/Fe^{3+}_{O_h} \rightarrow Co^{3+}_{O_h}/Fe^{2+}_{O_h}$, (2) $Co^{2+}_{O_h}/Fe^{3+}_{T_d} \rightarrow Co^{3+}_{O_h}/Fe^{2+}_{T_d}$, (3) $Co^{2+}_{T_d}/Fe^{3+}_{O_h} \rightarrow Co^{3+}_{T_d}/Fe^{2+}_{O_h}$, and (4) $Co^{2+}_{T_d}/Fe^{3+}_{T_d} \rightarrow Co^{3+}_{T_d}/Fe^{2+}_{T_d}$. The first two pathways account for possible metal-to-metal charge transfer transitions in the inverse spinel structure. The third pathway accounts for the only analogous transition in the normal spinel structure. The fourth pathway accounts for a transition in the partially inverse structure, which has the possibility of adjacent Co^{2+} and Fe^{3+} T_d centers. To simulate the excited state spectra for these possible excitation pathways, the same process as described above is performed starting with the appropriate multiplet structures for $Fe^{2+/3+}_{O_h/T_d}$ and $Co^{2+/3+}_{O_h/T_d}$ specific to each excited state. The relative contribution of these species to the excited state spectrum is weighted based on a variable excitation fraction. The ground state spectrum is then subtracted from the excited state spectrum to generate a simulated

transient XUV-RA spectrum.

As described in the main manuscript, we also consider the possibility for SCO on photoexcited Co^{3+}. Considering two different spin states for each of the four possible excitations pathways gives rise to eight potential excited state spectra, which are compared below. The spin state of the absorption centers can be controlled by changing the crystal field splitting (CFS) energy, which is added to the multiplet structure as a perturbation. For the simulated cobalt $M_{2,3}$-edge, HS $Co^{2+/3+}$ has a CFS energy of 1.20 eV[S18] and LS Co^{3+} has 8.00 eV. We found that this large increase in the CFS is required to reproduce the experimentally observed transient spectrum. All parameters for the HS simulations are summarized in Table S2. The LS simulations use exactly the same parameters, with the exception of the crystal field splitting. Note that a small energy offset has been applied to the multiplet simulations for each metal center in order to match the experimental transient features as is typical for these calculations[S12,S13,S16]; however, these energy offsets remain fixed across the excited state simulations compared below.

Table S2: LS $Co^{2+/3+}$ uses the same parameters as the HS simulation, with the exception of a crystal field splitting of 8.00 eV for the O_h and -8.00 eV for the T_d configurations, respectively.

	$Fe^{2+}_{O_h}$	$Fe^{2+}_{T_d}$	$Fe^{3+}_{O_h}$	$Fe^{3+}_{T_d}$	$Co^{2+}_{O_h}$	$Co^{2+}_{T_d}$	$Co^{3+}_{O_h}$	$Co^{3+}_{T_d}$
Crystal Field Splitting / eV	1.10	-0.60	1.45	-0.60	1.20	-1.20	1.20	-1.20
Slater Integral Reduction	50%	50%	50%	50%	60%	60%	60%	60%
Fano Parameter	3.5	3.5	4.7	4.7	4.0	4.0	2.2	2.2
Minimum Lorentzian Width / eV	0.1	0.1	0.1	0.1	0.1	0.1	0.1	0.1
Lorentzian Broadening / eV	0.42	0.42	0.42	0.42	0.42	0.42	0.42	0.42
Lorentzian Cutoff / eV	48	48	48	48	54	54	57	57
Energy Offset / eV	0.50	0.50	0.25	0.25	0.75	0.75	0	0

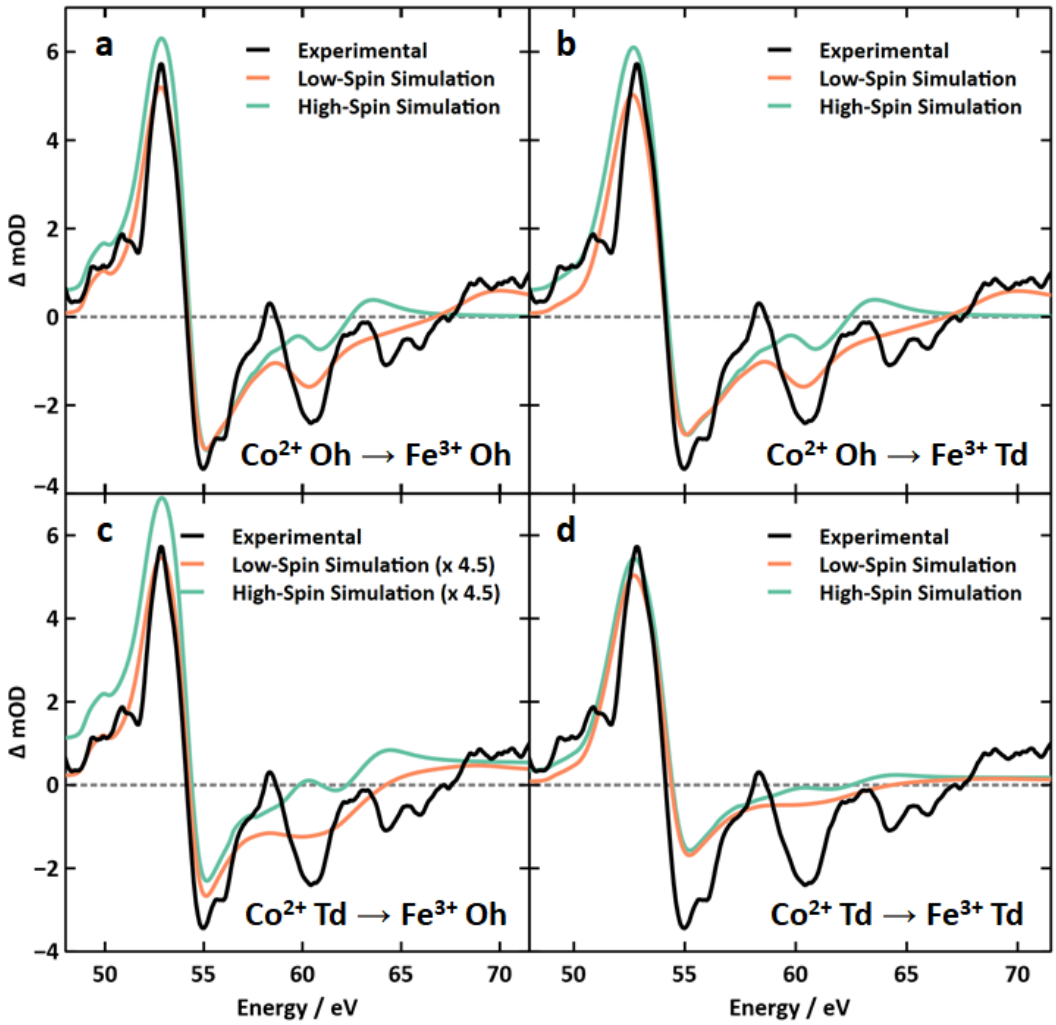

Figure S6: Simulated transient spectra for a perfectly HS (teal) and LS (orange) for the (a) $Co^{2+}_{O_h} \rightarrow Fe^{3+}_{O_h}$, (b) $Co^{2+}_{O_h} \rightarrow Fe^{3+}_{T_d}$, (c) $Co^{2+}_{T_d} \rightarrow Fe^{3+}_{O_h}$, and (d) $Co^{2+}_{T_d} \rightarrow Fe^{3+}_{T_d}$ excitation pathways. The $O_h \rightarrow O_h$ pathways matches best with the experimental results.

Figure S6 compares the experimental transient spectrum representing an average of time delays >400 fs (black) with the simulated transient spectra for each of the four possible metal-to-metal charge transfer transitions . In these simulations, LS Co^{3+} represents the result of SCO and are depicted in orange while HS Co^{3+} indicates the absence of spin crossover and are shown in teal. The HS simulations poorly match the experimental spectrum at the Co $M_{2,3}$-edge in all the excitation pathways. However, the LS simulations in Figures S6a and S6b closely resemble one another and agree well with the experimental data at the Co $M_{2,3}$-edge confirming a photoinduced spin crossover in the inverse spinel structure. The LS simulation

in Figure S6c corresponding to spin crossover in the normal spinel structure does not match the observed spectrum at the Co edge, missing a well-defined Co^{2+} bleach at 60.5 eV and a Co^{3+} excited state absorption at 69 eV. Figure S6d represents the worst of all possible fits to the experimental data, failing to reproduce the transient features at the both the Fe and Co $M_{2,3}$-edges.

From this we conclude that the photoexcited Co^{3+} is primarily LS and octahedrally coordinated. Seeking to differentiate between the $Co^{2+}_{O_h}/Fe^{3+}_{O_h} \rightarrow Co^{3+}_{O_h}/Fe^{2+}_{O_h}$ and $Co^{2+}_{O_h}/Fe^{3+}_{T_d} \rightarrow Co^{3+}_{O_h}/Fe^{2+}_{T_d}$ transitions, we observe that there is a shoulder present in the Fe $M_{2,3}$-edge around 50 eV in the experimental spectrum which is predicted by the $Fe^{3+}_{O_h}$ pathway (Figures S6a), but is notably missing for the $Fe^{3+}_{T_d}$ transition (Figures S6b). Therefore, we assume that the $Co^{2+}_{O_h}/Fe^{3+}_{O_h} \rightarrow Co^{3+}_{O_h}/Fe^{2+}_{O_h}$ transition pathway leading to SCO on photoexcited Co^{3+} is responsible for the observed experimental spectrum. As described in the main manuscript, this charge transfer assignment intuitively agrees well with the spinel crystal structure since the Co and Fe O_h metal centers in the inverse spinel would have the greatest degree of orbital overlap, having a shorter through-space coupling distance ($\sim$ 2.8 Å) as compared to the Co $O_h \rightarrow$ Fe T_d in the inverse spinel and Co $T_d \rightarrow$ Fe O_h in the normal spinel ($\sim$ 3.3 Å) or the Co $T_d \rightarrow$ Fe T_d mixed-phase pathway ($\sim$ 3.5 Å).

Using an excited state assignment based on the $Co^{2+}_{O_h}/Fe^{3+}_{O_h} \rightarrow Co^{3+}_{O_h}/Fe^{2+}_{O_h}$ transition, we added linear weightings corresponding to the percent excitation fraction and degree to which photoexcited Co^{3+} converts from HS to LS to the simulated excited state spectrum. These parameters were optimized using a nonlinear, least-squares regression analysis to calculate the total excitation fraction as well as the internal quantum efficiency for spin crossover. Results of this regression yield an excitation fraction of 1.1% and an internal quantum efficiency for spin crossover of unity (100 $\pm$ 3.4%). This spectrum corresponding to the $Co^{2+}_{O_h}/Fe^{3+}_{O_h} \rightarrow Co^{3+}_{O_h}/Fe^{2+}_{O_h}$ transition, accounting for excitation and spin crossover fraction, are shown in Figures 3b and 4c in the main manuscript.

References

(S1) Eskandari, F.; Porter, S.; Venkatesan, M.; Kameli, P.; Rode, K.; Coey, J. *Physical Review Materials* **2017**, *1*, 074413.

(S2) Waseda, Y.; Shinoda, K.; Sugiyama, K. *Zeitschrift für Naturforschung A* **1995**, *50*, 1199–1204.

(S3) Concas, G.; Spano, G.; Cannas, C.; Musinu, A.; Peddis, D.; Piccaluga, G. *Journal of Magnetism and Magnetic Materials* **2009**, *321*, 1893–1897.

(S4) Carta, D.; Casula, M. F.; Falqui, A.; Loche, D.; Mountjoy, G.; Sangregorio, C.; Corrias, A. *The Journal of Physical Chemistry C* **2009**, *113*, 8606–8615.

(S5) De Santis, M.; Bailly, A.; Coates, I.; Grenier, S.; Heckmann, O.; Hricovini, K.; Joly, Y.; Langlais, V.; Ramos, A. Y.; Richter, C. et al. *Acta Crystallographica Section B: Structural Science, Crystal Engineering and Materials* **2019**, *75*.

(S6) Yadav, R. S.; Kuřitka, I.; Vilcakova, J.; Havlica, J.; Masilko, J.; Kalina, L.; Tkacz, J.; Švec, J.; Enev, V.; Hajdúchová, M. *Advances in Natural Sciences: Nanoscience and Nanotechnology* **2017**, *8*, 045002.

(S7) Ravindra, A.; Padhan, P.; Prellier, W. *Applied Physics Letters* **2012**, *101*, 161902.

(S8) Holinsworth, B.; Mazumdar, D.; Sims, H.; Sun, Q.-C.; Yurtisigi, M.; Sarker, S.; Gupta, A.; Butler, W.; Musfeldt, J. *Applied Physics Letters* **2013**, *103*, 082406.

(S9) Sharma, D.; Khare, N. *AIP Advances* **2016**, *6*, 085005.

(S10) Matzen, S.; Moussy, J.-B.; Mattana, R.; Petroff, F.; Gatel, C.; Warot-Fonrose, B.; Cezar, J.; Barbier, A.; Arrio, M.-A.; Sainctavit, P. *Applied Physics Letters* **2011**, *99*, 052514.

(S11) Stavitski, E.; De Groot, F. M. *Micron* **2010**, *41*, 687–694.

(S12) Vura-Weis, J.; Jiang, C.-M.; Liu, C.; Gao, H.; Lucas, J. M.; De Groot, F. M.; Yang, P.; Alivisatos, A. P.; Leone, S. R. *The Journal of Physical Chemistry Letters* **2013**, *4*, 3667–3671.

(S13) Jiang, C.-M.; Baker, L. R.; Lucas, J. M.; Vura-Weis, J.; Alivisatos, A. P.; Leone, S. R. *The Journal of Physical Chemistry C* **2014**, *118*, 22774–22784.

(S14) Attwood, D.; Sakdinawat, A. *X-rays and extreme ultraviolet radiation: principles and applications*; Cambridge university press, 2017.

(S15) Kaplan, C. J.; Kraus, P. M.; Gullikson, E. M.; Borja, L.; Cushing, S. K.; Zürch, M.; Chang, H.-T.; Neumark, D. M.; Leone, S. R. *JOSA B* **2019**, *36*, 1716–1720.

(S16) Cirri, A.; Husek, J.; Biswas, S.; Baker, L. R. *The Journal of Physical Chemistry C* **2017**, *121*, 15861–15869.

(S17) Berlasso, R.; Dallera, C.; Borgatti, F.; Vozzi, C.; Sansone, G.; Stagira, S.; Nisoli, M.; Ghiringhelli, G.; Villoresi, P.; Poletto, L. et al. *Physical Review B* **2006**, *73*, 115101.

(S18) Moyer, J.; Vaz, C.; Negusse, E.; Arena, D.; Henrich, V. *Physical Review B* **2011**, *83*, 035121.